JGR Oceans

RESEARCH ARTICLE
10.1029/2020JC016522

Drivers of Interannual Sea Ice Concentration Variability in the Atlantic Water Inflow Region North of Svalbard

Øyvind Lundesgaard[1], Arild Sundfjord[1], and Angelika H. H. Renner[2]

[1]Norwegian Polar Institute, Fram Centre, Tromsø, Norway, [2]Institute of Marine Research, Fram Centre, Tromsø, Norway

Key Points:

- Ocean heat maintains ice-free conditions in the Atlantic Water inflow region during autumn/winter
- Interannual sea ice variability was *not* driven by changes in ocean heat during 2012–2019
- Anomalous sea ice years were associated with anomalies in atmospheric circulation and ice advection

Supporting Information:

Supporting Information may be found in the online version of this article.

Correspondence to:

Ø. Lundesgaard,
oyvind.lundesgaard@npolar.no

Citation:

Lundesgaard, Ø., Sundfjord, A., & Renner, A. H. H. (2021). Drivers of interannual sea ice concentration variability in the Atlantic Water inflow region north of Svalbard. *Journal of Geophysical Research: Oceans*, *126*, e2020JC016522. https://doi.org/10.1029/2020JC016522

Received 19 JUN 2020
Accepted 13 MAR 2021

Abstract Sea ice concentration along the continental margin of the Arctic Ocean is influenced by a multitude of factors, including local freezing and melting due to atmospheric forcing, lateral advection of sea ice by winds and ocean currents, and melting from below by warm Atlantic Water (AW). Here, we characterize the evolution of sea ice concentration in an area on the continental shelf break north of Svalbard in the period between 2012 and 2019. During this period, a semi-regular seasonal pattern in sea ice concentration was interrupted by three anomalous seasons; a high ice anomaly during autumn 2014 and low ice anomalies during spring 2016 and 2018. Neither type of anomaly can be explained by abnormal upper ocean heat content as measured by an ocean mooring located near the shelf break. Instead, we find that the predominant driver of interannual sea ice concentration variability during this period was variations in large-scale ice drift. While heat flux from the ocean cannot explain the interannual variability, it plays a key role in maintaining periods of open water in the AW inflow region despite freezing air temperatures during most of the year. These results are consistent with the sea ice concentration flux divergence from satellite records, which suggests that the southern continental slope of the Eurasian Basin is an important melting area for sea ice advected in from the north.

Plain Language Summary Atlantic Water flows from the Nordic Seas into the Arctic Ocean, where it forms a warm ocean current running along the continental slope. At the beginning of this current, in the region north of Svalbard, the warm upper ocean maintains the ocean ice-free during parts of the year where sea ice otherwise would have formed. The goal of this study was to investigate whether years with a particularly large or small amount of ice in this region occur as a result of unusually high or low ocean temperature. We examined records of temperature from instruments moored in the ocean northeast of Svalbard between 2012 and 2019. We compared these observations with the satellite record of sea ice concentration, along with other variables including air temperature and sea ice movement. Our findings suggest that ocean heat strongly influences sea ice concentration by melting ice and preventing new ice from forming, but that large year-to-year sea ice variations were not a result of variations in ocean temperature. Instead, unusual sea ice years were associated with unusual large-scale wind patterns, which in turn control air temperature and moisture and movement of sea ice into the area from other parts of the Arctic Ocean.

1. Introduction

The fraction of the Arctic Ocean that is covered by sea ice is declining; annual mean sea ice area in the northern hemisphere decreased at a rate of approximately 4.5% per decade between 1979 and 2015 (Comiso et al. [2017]; see also J. Stroeve and Notz [2018] and Kwok [2018]). The details of this strong overall trend are complex, and include spatial inhomogeneities as well as substantial interannual variability (Onarheim et al., 2018; Serreze & Stroeve, 2015). Many physical processes impact sea ice concentration (*SIC*), and different forcing mechanisms may determine local SIC in different areas, and on different temporal and spatial scales (England et al., 2019; Perovich & Richter-Menge, 2015). Local case studies are therefore an important supplement to the large-scale pan-Arctic picture of sea ice evolution.

The area north and northeast of Svalbard has experienced a loss of sea ice in both spring and autumn during the satellite era (Onarheim et al., 2014, 2018), but it is also a regional maximum of interannual variability (Grunseich & Wang, 2016, present study). In the 21st century, the spring ice-free area north of Svalbard has expanded eastward (Ivanov et al., 2015; Tetzlaff et al., 2014), along the pathway of relatively warm Atlantic

Water (AW). AW is transported through the eastern Fram Strait with the West Spitsbergen Current (*WSC*), wraps around the northwestern tip of Spitsbergen in three separate branches, and ultimately converges along the continental margin as the warm Fram Strait branch of the Atlantic Water Boundary Current in the Arctic Ocean (*FSAW*), centered near the 700 m isobath (Koenig et al., 2017; Menze et al., 2019). In contrast to most of the Arctic Ocean, where AW is separated from the sea surface by a strong halocline layer (Aagaard et al., 1981), AW is often found at or in close proximity to the surface in the area north of Svalbard (Meyer et al., 2018; Renner et al., 2018). As a result, the region experiences large ocean-atmosphere heat fluxes in autumn and winter (Cokelet et al., 2008), and it is a region where variability in ocean heat content has the potential to impact the sea ice cover directly (e.g., Ivanov et al., 2015; V. V. Ivanov & Repina, 2018; Onarheim et al., 2014; Polyakov et al., 2017). However, it is not clear to what extent the high interannual variability in sea ice cover is a result of variable oceanic forcing.

Interannual sea ice variability in the Arctic Ocean as a whole is primarily driven by variations in surface air temperature (*SAT*; Olonscheck et al., 2019; Serreze & Stroeve, 2015). Such variations are in turn governed by a complex set of drivers and interactions; Arctic SAT variability is closely linked to large-scale climate modes of variability like the Arctic Oscillation (Moritz et al., 2002; Rigor et al., 2002), and to various feedback mechanisms involving, among others, sea ice albedo, ocean-air heat fluxes, and cloud formation (Serreze & Barry, 2011). The large incidence of cyclones in the Atlantic sector of the Arctic Ocean impact sea ice by reducing ocean-atmosphere heat loss as a result of heat and moisture transport (Rinke et al., 2017; Sorteberg & Walsh, 2008), but also by increasing snowfall and mechanical fracturing of sea ice by strong winds (Graham et al., 2019; Merkouriadi et al., 2020). Furthermore, variations in atmospheric circulation can alter the spatial distribution of sea ice by impacting large-scale patterns of sea ice drift, and thereby have important regional impacts on SIC in the marginal sea ice zone of the Arctic Ocean (e.g., Kimura et al., 2013; Kwok, 2015; Lind et al., 2018).

This study examines drivers of sea ice variability in the AW inflow pathway northeast of Svalbard. We add to the previous studies listed above by jointly analyzing the observed interannual variability of sea ice, ocean and atmosphere, focusing on a particular location that has recently transitioned into being seasonally ice-free, and on a seven-year period (2012–2019) when sea ice conditions varied greatly. The study uses satellite and reanalysis data in combination with what to our knowledge is the longest existing ocean time series from the Atlantic Water inflow region east of the Yermak Plateau, collected from an ocean mooring on the upper continental margin at 31.5°E. We consider three main factors that undoubtedly impact SIC in this region, and that may exhibit considerable interannual variability: the temperature of the underlying ocean, which is strongly affected by heat transport into the area by the WSC (Kawasaki & Hasumi, 2016; Muilwijk et al., 2018), the atmospheric conditions around Svalbard (Gjelten et al., 2016; Nordli et al., 2014), and the large-scale patterns of Arctic Ocean sea ice drift (Kaur et al., 2018; Krumpen et al., 2019). Empirically derived insights into the processes governing sea ice variability are essential in order to understand and model the coupled atmosphere-ice-ocean system in this region, and predict how it may evolve in the future in a continually changing oceanic and atmospheric climate.

2. Data and Methods

2.1. Ocean Mooring

Upper ocean observations used in this study were mainly obtained from an ocean mooring deployed at 81°24.2′N, 31°13.2′E near the continental shelf break north of Kvitøya toward the Nansen Basin (Figure 1a) as part of the project *Long-term variability and trends in the Atlantic Water inflow region (A-TWAIN)*. Bottom depth at the mooring location is approximately 200 m. This mooring, which we will hereafter refer to as the *shelf break mooring*, was first deployed in September 2012, and it was serviced and redeployed in the same location in September of 2013, 2015, and 2017 (Table 1). Results from the 2012 to 2013 deployment have previously been presented in Renner et al. (2018) and Pérez-Hernández et al. (2019).

The shelf break mooring was equipped with SeaBird SBE37 and SBE16plus conductivity-temperature-pressure (CTD) sensors located at various depths during the different deployments. An overview of the sensors is shown in Table 1, and further details about the data and processing can be found in Text S1. The instruments were calibrated prior to deployment in 2012, with the exception two of the sensors operating during

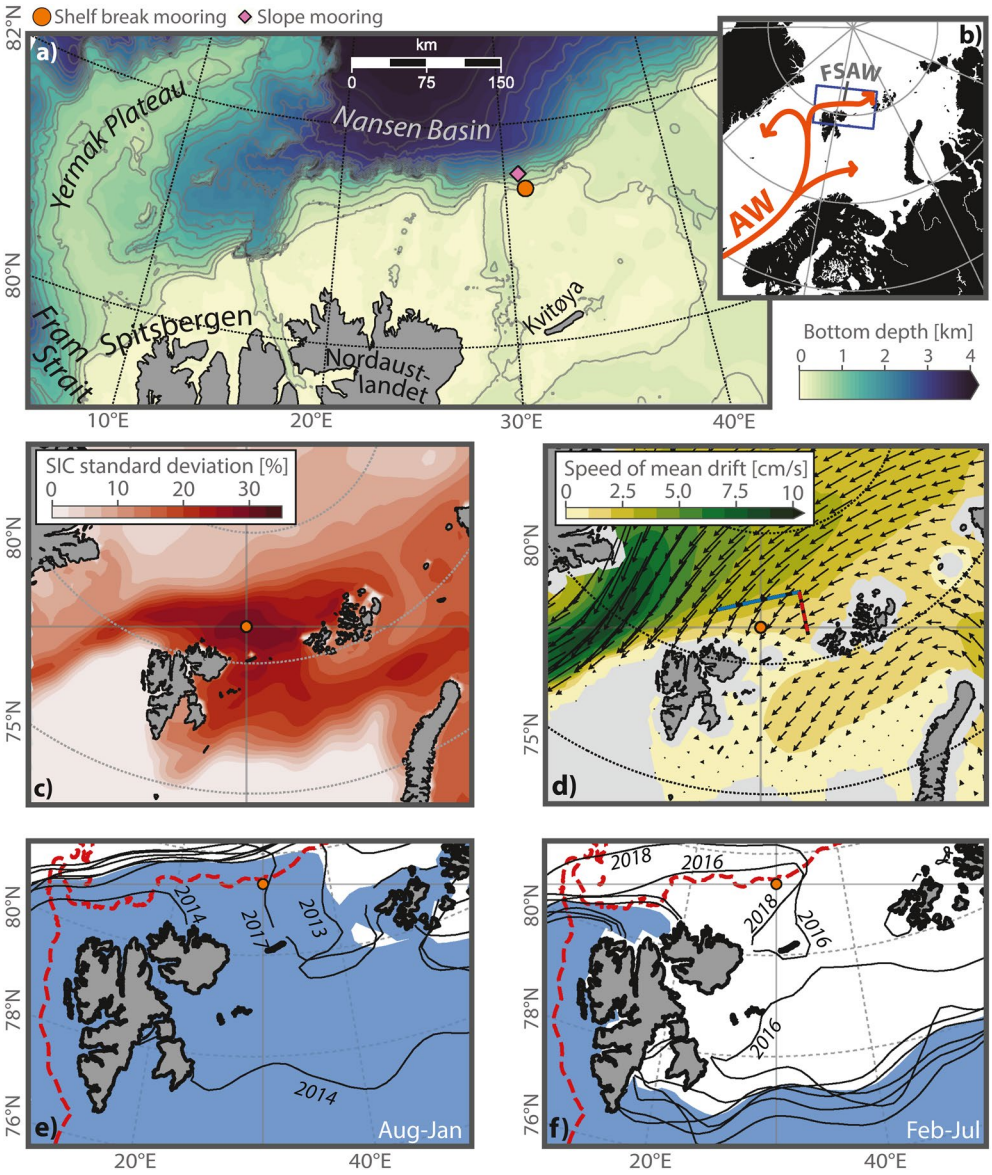

Figure 1. (a) Mooring locations with bathymetry from IBCAO v3 500 × 500 m (Jakobsson et al., 2012). Contours are separated by 250 m. (b) Overview map and schematic of main Atlantic Water pathways, and location of the FSAW. Rectangular box shows the location of the map in (a). (c) Standard deviation of monthly averaged NSIDC SIC from October 2012 through September 2019, after the interannual monthly mean has been subtracted. (d) Mean sea ice drift over the same period, from the NSIDC SID product. Quiver arrows indicate the speed and direction, and are subsampled at every third grid point. Dashed lines show flux gates *N* (blue) and *E* (red). (e and f) Extent of 30% average NSIDC SIC during August–January (e) and February–July (f). White color on blue background shows the seasonal averages between August 1, 2012 and July 31, 2019. Black contours show the extent for each individual season. Anomalous years are indicated with a label near the associated contour (label defined by the year of the first month of the season). Red dashed lines show the 700 m depth contour, a proxy for the pathway of AW transport. Orange circle and intersection of gray lines show the shelf break mooring location in (c–f).

the final deployment; a SBE16plus at 44 m depth and one SBE37 at 108 m depth were both calibrated in 2016. For analysis, the records from the sensors were interpolated to a common 10-min time grid before further processing was applied, in order to ensure consistency between the time series from the various deployments. Furthermore, the records were linearly interpolated in depth to obtain fixed-depth time series from 63 and 107 m in order to examine trends over the study period.

Table 1
Overview of Deployments of the Shelf Break and Slope Ocean Moorings With Median Depth of SBE37 CTD Sensors Used in This Study

Shelf break	Deployment 1	Deployment 2	Deployment 3	Deployment 4
Dates	16.09.2012–15.09.2013	21.09.2013–15.09.2015	19.09.2015–17.09.2017	21.09.2017–18.11.2019
Duration [days]	364	724	729	789
Sensor depths [m]	104 m, 132 m	46, 111, 137	49, 129	44[a], 67, 108
Slope	**Deployment 1**	**Deployment 2**		
Dates	18.09.2012–16.09.2013	22.09.2013–15.09.2015		
Duration [days]	363	726		
Sensor depths [m]	94	102		

[a]SBE16plus Sensor, record extends from 01.10.2017 to 02.06.2019.

The location of the shelf break mooring allows us to examine the upper ocean conditions up-slope of the core of the AW boundary current (Pérez-Hernández et al., 2019). In addition, this study also uses ocean temperature data from another A-TWAIN mooring, hereafter referred to as the *slope mooring*, which was located 17 km further north at 81°32.6′N, 30°51.4′E. At approximately 800 m bottom depth, this mooring was located near the center of the FSAW inflow, and therefore enables us to compare the upper ocean conditions at the shelf break with those in the core of the AW inflow. Data from this mooring is only available from the first and second deployments (2012–2015); the mooring was lost during both subsequent deployment periods. This study only uses data from a SBE37 temperature sensor mounted near 100 m depth on the slope mooring, in order to compare with the ocean temperatures measured on the shelf break. Due to the combination of stronger currents and a longer mooring wire, this temperature sensor experienced larger excursions from its mean depth than those on the shelf break mooring. In order to avoid erroneously interpreting vertical displacements as temporal variability, we disregarded temperature measurements obtained further than 20 m from the deployment median depth. Since the shelf break mooring provides the longest record, it is the the main focus of this study, and we define the location of the shelf break mooring as the main study site.

Data from the four mooring deployments are openly accessible at the Norwegian Polar Data Center (Sundfjord et al., 2017, 2020; Lundesgaard et al., 2020a, 2020b).

2.2. Sea Ice and Atmosphere Data Products

For the purpose of analysis, we split the year up into two halves, August-January and February-July, where each individual season is denoted by the year of its starting month. As shown in Figure S2, and Section 3.1.1, the August-January and February-July seasons approximately correspond to the low and high SIC seasons in the study area, respectively.

We obtained local time series of sea ice and atmospheric variables from various gridded surface data sets. All surface variables extracted from large-scale data products were bilinearly interpolated onto the coordinates of the shelf break mooring location. Air temperature at 2-m elevation and latent, sensible, and radiative surface heat fluxes were extracted from the ECMWF ERA-5 global reanalysis product (Copernicus Climate Change Service [C3S], 2017). A recent analysis by Wang et al. (2019) shows that although this product is subject to certain biases over sea ice, it generally performs better than its widely used predecessor ERA-Interim over the Arctic Ocean.

In order to obtain an approximate index of the amount of local thermodynamic ice growth, we computed the accumulation of freezing degree days (*FDD*) for each season:

$$FDD = \sum_i \left((-1.8°\mathrm{C}) - T_i\right) \mathcal{H}\left((-1.8°\mathrm{C}) - T_i\right) \Delta t \quad (1)$$

where T_i is the daily average local ERA-5 2-m air temperature, $\Delta t = 1$ day, and the sum is over all days within the season. $\mathcal{H}(x)$ is 1 for positive x, and zero elsewhere.

Sea ice drift (SID) was obtained from the National Snow and Ice Data Center Polar Pathfinder Daily 25 km EASE-Grid Sea Ice Motion Vectors product (Tschudi et al., 2019, hereafter *NSIDC SID*), which extends from 1978 to present. Sea ice thickness (SIT) was obtained from the *CS2SMOS* blended product of thickness estimates from CryoSat 2 and SMOS provided by the Alfred Wegener Institute (Ricker, Hendricks, Kaleschke, et al., 2017). CS2SMOS provides weekly averaged SIT on a 25 × 25 km grid from November 2010 onward, and is only available during parts of the year (Oct-Nov to Mar-Apr).

Sea ice concentration (SIC) was obtained from the *Sea Ice Concentrations from Nimbus-7 SMMR and DMSP SSM/I-SSMIS Passive Microwave Data, Version 1* product from NSIDC (Cavalieri et al., 1996, hereafter *NSIDC SIC*). The product has a uniform spatial resolution of 25 km. Daily SIC is provided every 2 days until August 20, 1987 (NIMBUS-7) and every day from August 21, 1987 (DMSP). In this study, the temporal resolution during the NIMBUS-7 period was increased to daily by averaging between adjacent days. In addition, 41-day gap in December-January 1987 was filled using linear interpolation. A comparison with the University of Bremen daily SIC product from the Advanced Microwave Scanning Radiometer 2 based on the ASI algorithm (Spreen et al., 2008) showed that NSIDC SIC generally produces somewhat lower ice concentrations in the study area (Text S2), but the main results of this study are not sensitive to the choice of SIC product.

In order to obtain an index of sea ice advection into the area, we computed the sea ice area flux across two flux gates labeled *N gate* and *E gate* (Figure 1d). Both were oriented in the diagonal direction of the NSIDC SID grid. Although not oriented along lines of constant latitude or longitude, the 177 km long E gate captures westward drift into the study area along the slope region northwest of Franz Josef Land, while the 353 km long N gate captures drift into the study area from the north. Sea ice area flux across each gate was computed at daily intervals by multiplying the daily mean NSIDC SID drift velocity in the cross-gate direction at each grid point of the gate with NSIDC SIC (the latter bilinearly interpolated onto the grid of the former). Net flux was calculated by integrating the flux across all grid points of each gate.

3. Results

3.1. Ice, Ocean, and Atmosphere During 2012–2019

3.1.1. Sea Ice Concentration and Thickness

The shelf break mooring was situated in an area of high seasonal and interannual SIC variability (Figures 1c, 1e, and 1f). The average sea ice edge (operationally defined here as the NSIDC 30% SIC contour) in the August-January seasons during the study period was located north of the continental slope. In the February-July seasons, the average sea ice edge extended westward past 20°E north of Svalbard, as well as across much of the northern Barents Sea. Sea ice extent also exhibited significant interannual variability. In particular, August-January of 2014 stood out as a period of anomalously high SIC relative to the interannual mean, and February-July of 2016 and 2018 were periods of anomalously low SIC (Figures 1e and 1f). These regional SIC anomalies were also reflected locally at the shelf break mooring location (Figure 2a).

In the anomalous season of August-January 2014, the mean sea ice edge along the AW inflow pathway north of Svalbard was situated near 20°E, approximately 20° west of its typical August-January location (Figure 1e). The sea ice cover also extended across the northern Barents Sea, which during other years was largely ice free in autumn. Monthly average SIC in the study region at the shelf break mooring remained above 50% during the whole period, and the study site never became entirely ice-free in 2014 (Figure 2a).

In February–July of both 2016 and 2018, the mean sea ice edge was displaced eastward from its typical location, with <30% SIC over the entire continental shelf north of Svalbard (Figure 1f). This included the shelf break mooring location, where mean SIC was much lower during the February–July seasons of 2016 and 2018 (<20%) compared to the four other years (64%–85%, Figure 2a).

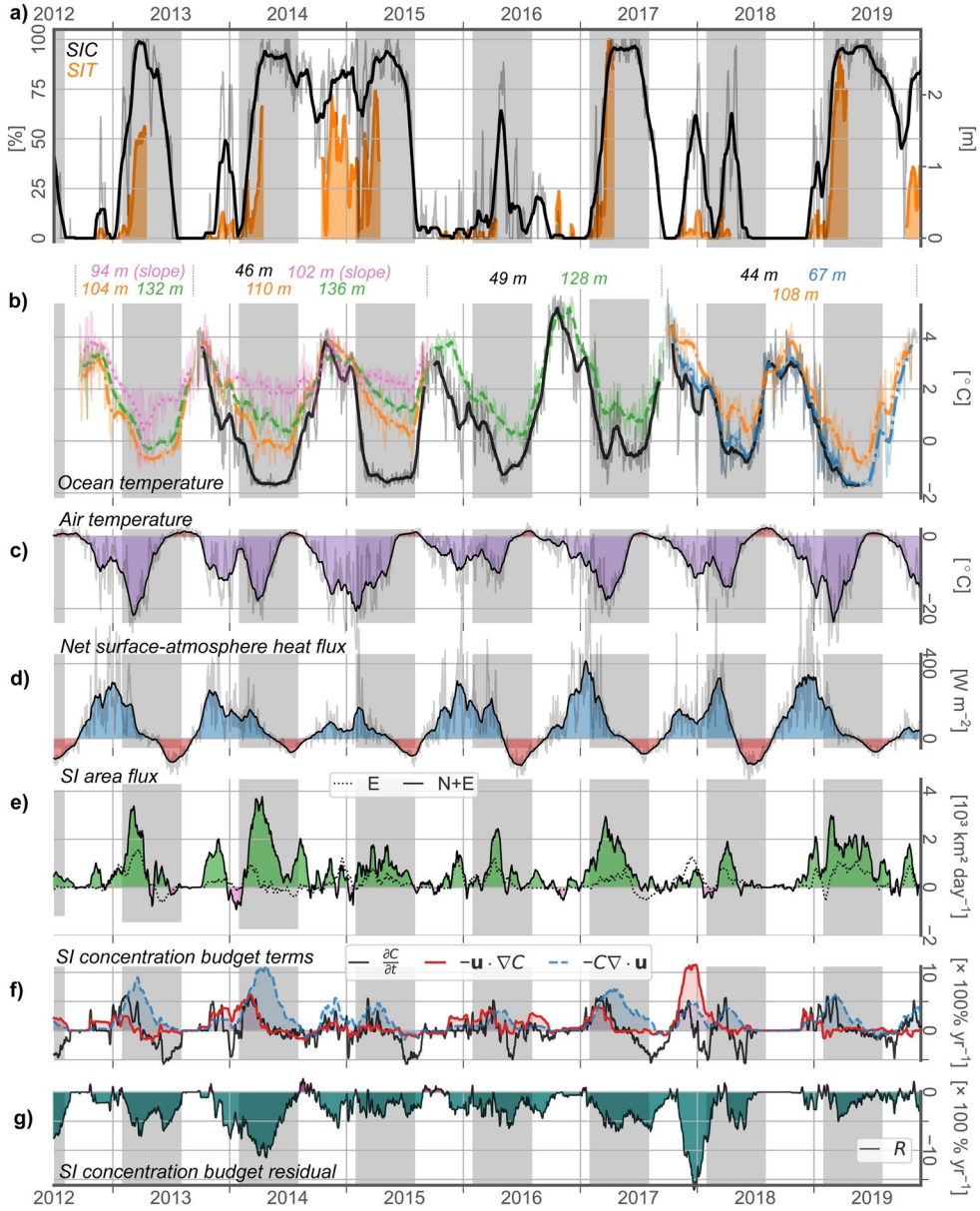

Figure 2. Time series of various variables at the shelf break mooring location. Gray background shading denotes high SIC seasons. (a) Sea ice concentration (black) and sea ice thickness (orange). (b) Ocean temperature from the various sensors (text labels above show deployment median depth). (c) 2-m air temperature. (d) Net ocean-atmosphere heat flux. (e) Net sea ice drift across the large scale transects shown in Figure 1c, positive toward the mooring site. Dotted lines show the net flux only through the E gate. (f) Three first terms of Equation 2. All terms are defined such that positive values indicate SIC increase. (g) Like (f), for the residual term of Equation 2, which represents SIC change due to freezing/melting and deformation. (a–e) Show 31-day running averages (thick lines) and daily means (thin faint lines). (f and g) Show 61-day running averages.

Local CS2SMOS sea ice thickness (Figure 2a) largely mirrored the evolution of sea ice concentration through the study period. In 2013, 2014, 2017, and 2019, SIT rose abruptly (to between 1.0 and 2.5 m) along with the increase in SIC during the early months of the year. In the low-SIC growth seasons of 2016 and 2018, SIT remained below 0.5 m. In the high-SIC autumn of 2014, SIT was already ~1 m at the start of the record in October.

3.1.2. Ocean Conditions

Subsurface ocean temperature at the shelf break mooring exhibited a strong seasonality, typically with a peaked maximum around September-October and a broader minimum in March-July (Figure 2b). Average temperatures during the August-January seasons (interpolated between sensors to a constant depth) were 2.48 °C at 63 m (2014–2018) and 2.88 °C at 107 m (2013–2018). The average temperatures during the February-July seasons were − 0.20 °C at 63 m (2014–2019) and 0.49 °C at 107 m (2013–2019).

Temperature generally increased with depth; during the seasons where a shallow sensor was available, interpolated ocean temperature was higher at 107 m than at 63 m, by, on average, 0.49 °C in August-January (2014–2018) and 0.93 °C in February-July (2014–2019). This vertical temperature difference nearly vanished near the annual temperature maximum, and was greatest during the annual minimum, consistent with strong heat loss from the uppermost part of the water column during winter.

The seasonal cycle was less pronounced at the slope mooring, in the center of the FSAW inflow. Seasonal maximum temperatures were similar to those at the shelf break (∼3 °C), but during February-July, there was a 1 °C–2 °C temperature increase from the shelf break to the slope mooring near 100 m depth.

Near the seasonal temperature maximum, the potential temperature-salinity ($\theta - S$) distribution was centered within the bounds defined for AW ($\theta > 2$ °C, 27.7 kg m^{-3} < σ_θ < 27.97 kg m^{-3}, Rudels et al., 2005) for all sensors (Figure S1). In the February-July season, the $\theta - S$ distribution at the slope mooring near 100 m depth remained largely within the AW bounds, while waters were significantly colder at similar depths at the shelf break. At the ∼50 m deep sensor at the shelf break mooring, the February-July $\theta - S$ distribution aligned to a large degree with the salinity-dependent freezing point line, suggesting that surface cooling and/or freezing exerted a large influence on the shelf break water column down to this depth.

During the final deployment, sensors were in place near both 44 and 67 m. Temperatures at these two depths were closely aligned through most of October 2017 to June 2019 during both the seasonal maxima and minima, including a drop to near-freezing temperatures in April 2019.

Annual minimum temperatures at the shelf break mooring varied substantially between the years of the study period. Near 50 m depth, temperatures were near freezing for extended periods of time during ice-covered periods in 2014, 2015, and 2019. This was not the case between 2016 and 2018, including a period of high SIC in 2017. Average February-July temperature interpolated to 63 m depth increased each year between 2014 and 2018 at a mean rate of 0.34 °C year^{-1} (Figure 3), before dropping again the following year. A similar evolution was found in temperature at 107 m, but with a positive anomaly from the mean 2013–2018 increase (0.27 °C year^{-1}) during 2015. August-January temperatures were more variable during the study period, with a clear maximum in 2016 at both 63 and 107 m. The warmest month in the time series was October 2016, with monthly average ocean temperature >4.7 °C at both interpolated depths.

3.1.3. Air Temperature and Surface Heat Fluxes

Near-surface air temperature at the mooring location exhibited clear seasonality during the study period (Figure 2c). During all years, monthly averaged air temperature (°C) was positive in summer (somewhere between June and August), and in most years air temperatures reached a clear minimum in winter/spring. Annual mean temperature had maxima in the low SIC years 2016 (−3.4 °C) and 2018 (−4.8 °C) and minima in the high SIC years 2014 (−7.6 °C) and 2019 (−8.8 °C). Interannual differences were greatest in winter, and minimum monthly averaged air temperature was higher in the low sea ice years (−10.2 °C in 2016, and −14.0 °C in 2018) than in the remaining years (−17.7 °C to −23.7 °C).

The interannual variations in air temperature were reflected in the local accumulation of FDD (Figure 3). FDD had a distinct interannual maximum in August-January 2014 (1532 °C day compared to a mean of 654 °C day during August-January all other years 2013–2018), and a interannual minimum in February-July 2016 (568 °C day) and 2018 (832 °C day) compared to a mean of 1248 °C day during February-July all other years 2013–2019.

Net surface heat flux at the shelf break mooring location, calculated from ERA-5 variables as the sum of latent and sensible heat fluxes and shortwave and longwave radiation, is shown in Figure 2d. During all years, the annual mean surface heat balance was negative, with a short summer period dominated by downward

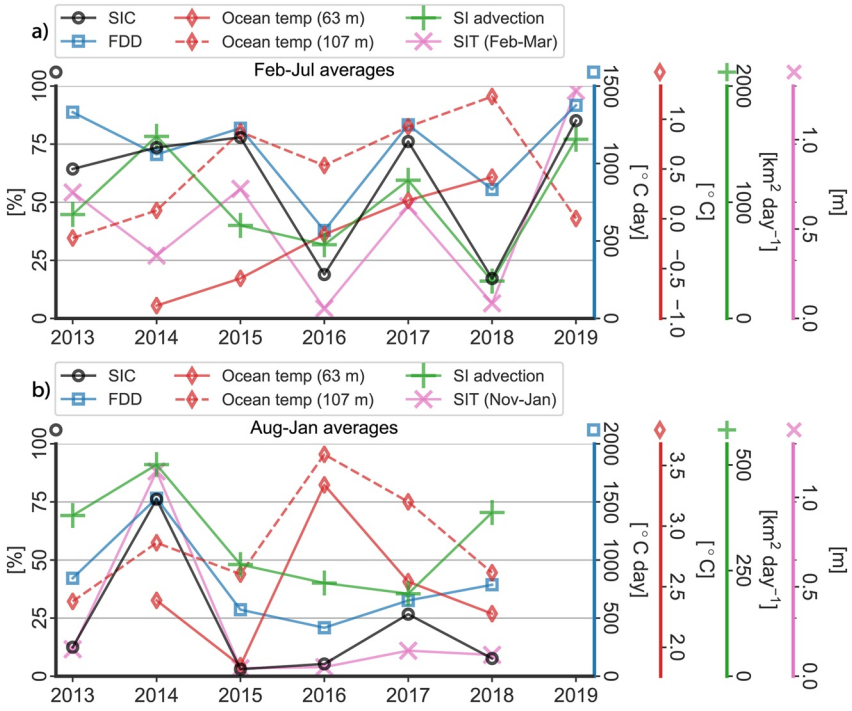

Figure 3. Seasonal average quantities from (a) August through January and (b) February through July.

shortwave radiation, and an extended winter period with heat loss from the surface to the atmosphere. Seasonal mean net upward surface heat flux was 109 W m^{-2} for the August-January seasons (2012–2018), and 23 W m^{-2} for the Feb-Jul seasons (2013–2019). Heat loss was greatest over a partially or wholly ice-free ocean; the sensible and latent heat flux contributions were greatly reduced during ice-covered conditions.

As shown in Figure 2, there were extended periods during which the ocean was largely ice-free while at the same time ocean heat was being lost to the atmosphere. During all years (July through June) except 2014/2015, the combination of surface heat loss and < 30% NSIDC SIC occurred during more than one third of the year; there were from 129 to 153 such days in the years starting in August 2012, 2013, 2016, 2017, and 2018, and 206 such days during the year starting August 2015. In the anomalously high SIC year starting in August 2014, there were only 6 days with < 30% SIC and upward surface heat flux.

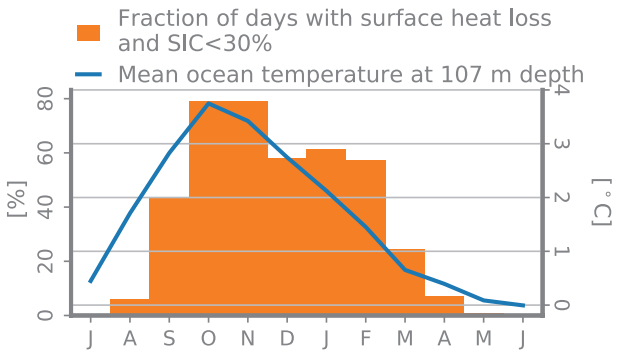

Figure 4. Mean seasonal cycles from the shelf break mooring location (October 2012 through September 2019). *Orange bars*: Fraction of days of the month where (i) daily net surface heat flux was directed from the ocean to the atmosphere, and (ii) daily average SIC was less than 30%. *Blue line*: Interannual mean monthly ocean temperature at 107 m depth.

Heat loss from the largely ice-free ocean to the atmosphere was generally greatest between October and February, when upper ocean temperatures were high and decreasing from the fall maximum (Figure 4). The extended periods of low SIC during active heat loss to the atmosphere are consistent with ocean heat preventing ice formation and delaying the onset of local sea ice cover. The implied amount of heat lost from the upper ocean is substantial; the annual heat loss to the atmosphere (integrated daily upward heat flux component from August through July) was between 2.6 and 3.5 GJ m^{-2} for all years between August 2012 and August 2019, with the exception of a clear minimum of 1.3 GJ m^{-2} during 2014/2015. For reference, a 3.0 GJ m^{-2} heat loss would reduce the mean temperature in a 100 m tall (stationary) water column by ~7.6 °C.

3.1.4. Sea Ice Drift

The study site was located outside the main pathway of the Transpolar Drift Stream (TDS), and sea ice was generally advected toward the site from the north and east (Figure 1c). Consequently, sea ice area advection across the two flux gates was predominantly oriented toward the study

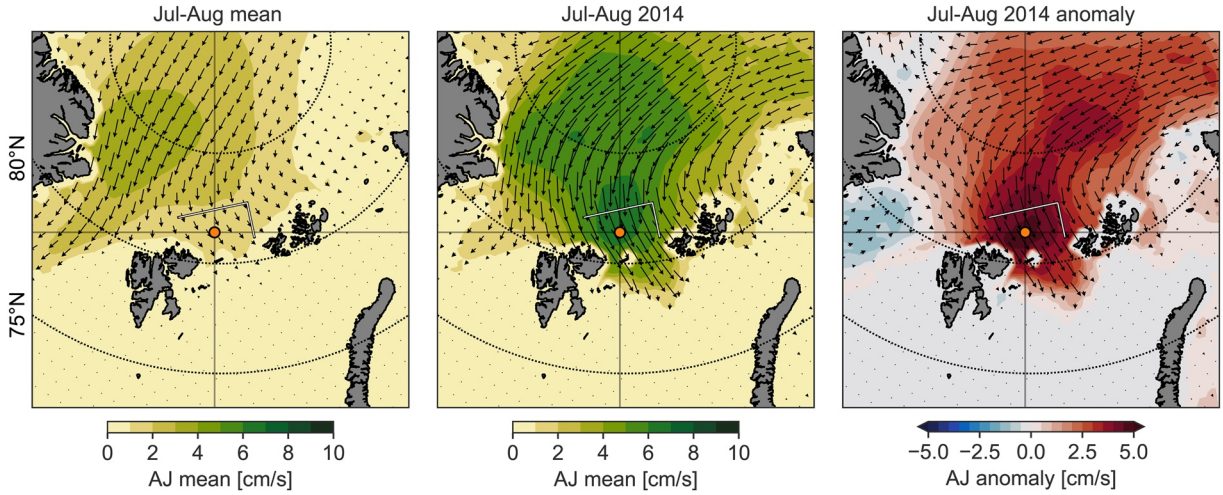

Figure 5. Mean sea ice drift in July through August: (a) Mean for 2012 through 2019. (b) Mean for the 2014. (c) (b) minus (a). White lines show the sea ice area flux gates.

site (Figure 2e). From October 2012 through September 2019, the mean net area flux toward the study site across the N and E gates were 15.0×10^4 and 7.1×10^4 km^2 year^{-1}, respectively.

Sea ice advection across the transect was seasonally skewed toward the February-July season. Generally, it was concentrated in intraseasonal pulses near the onset of the sea ice cover period in late winter/early spring, but there was considerable interannual variability. Notable maxima in sea ice area flux (average >1,100 km^2 day^{-1}) during the February-July seasons occurred in 2014, 2017, and 2019—all of which were dominated by flux through the N gate.

The net flux during the August-January season also had a clear maximum in 2014 (~500 km^2 day^{-1}). This unusually large inflow of sea ice area was in part due to an unusually timed advection episode which began in July 2014 and lasted through August, during what is typically the melt season (Figure 2e). During this time, there was a strong southward sea ice drift in the western Eurasian Basin of the Arctic Ocean (Figure 5), with the TDS intensifying and curving to the left, away from its usual outlet in the Fram Strait and instead toward the Barents Sea.

3.2. Sea Ice Concentration Budget

Having considered the characteristics of the various time series, we then examined patterns of SIC loss and gain by constructing a "sea ice concentration budget" for the broader area. We followed the methodology developed by Holland and Kimura (2016), decomposing the time (t) evolution of the local sea ice concentration for each spatial point, denoted by the subscript i:

$$\underbrace{\frac{\partial C_i}{\partial t}}_{\text{Intensification}} = \underbrace{-\mathbf{u}_i \cdot \nabla C_i}_{\text{Advection}} \underbrace{- C_i \nabla \cdot \mathbf{u}_i}_{\text{Convergence}} + \underbrace{R_i}_{\text{Residual}} \tag{2}$$

where C denotes the sea ice concentration, $\mathbf{u}$ is the local drift vector, and R_i is a residual which includes local sea ice concentration changes due to local freezing, melting and deformation (for example ridging). Equation 2 was evaluated daily at each point of the native 25 × 25 km grid of the NSIDC SID product, from which we obtained $\mathbf{u}$. C was obtained from NSIDC SIC bilinearly interpolated onto the NSIDC SID grid. Masked areas (land masks and no sea ice cover) were set to zero, $\mathbf{u}$ components were smoothed with a 3-point boxcar filter in both spatial directions in order to suppress grid-scale noise, and all calculations were otherwise performed as in Holland and Kimura (2016).

SIC is not a conservative property - unlike sea ice mass, the flux divergence of concentration cannot be considered in balance with a single melting/freezing term (see also Holland & Kimura, 2016; Petty et al., 2018).

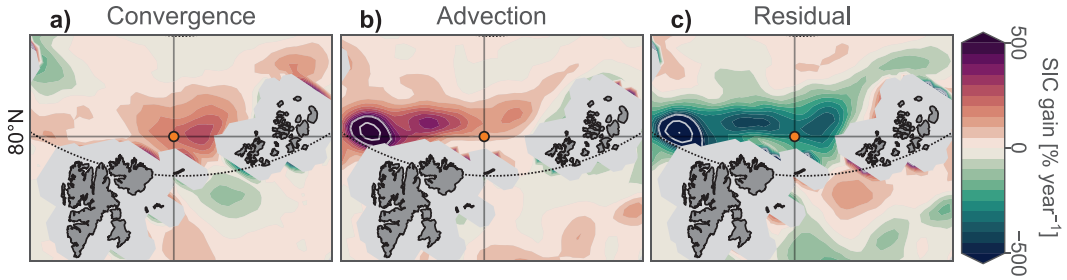

Figure 6. Average terms of Equation 2 from October 2012 through September 2019: (a) Convergence, $-C\nabla \cdot \mathbf{u}$, (b) advection, $-\mathbf{u} \cdot \nabla C$, and (c) residual, R. All terms are defined such that positive values (red) indicate SIC *gain*, and negative values (green) indicate SIC *loss*. Color scale saturated at ±500% year^{-1}; beyond this, white contours are shown at intervals of 250% year^{-1}. The absolute value of the average intensification term, $\frac{\partial C}{\partial t}$, was within ±15% year^{-1} everywhere in the domain.

In addition, errors and uncertainties are highest near the sea ice edge, and the 15% SIC cutoff of the NSIDC SID product implies that only ice at concentrations above this value is taken into account in the flux divergence terms. Yet, the methodology provides a useful means of identifying sea ice area sources and sinks, and of studying how these change over time.

Over seasonal time scales, the flux divergence terms (advection and convergence in Equation 2) were larger than the intensification, suggesting that the observed change in SIC did not balance the transport of sea ice area into the region. Moreover, the net flux divergence was negative (positive convergence), indicating that more sea ice area was advected into the region than out of it. Typically, the advection term peaked during the seasonal increase in SIC, followed within a few months by a peak in convergence (Figure 2f). The residual term (Figure 2g) was negative throughout most of the record, with a mean of −302% per year between October 2012 and September 2019. Assuming that the influence of ridging and other forms of deformation was minor, the analysis suggests that the study area was a sink of sea ice collected in the region by large-scale sea ice drift.

Clear spatial patterns emerge when the long-term SIC budget is considered over the greater region surrounding the mooring site (Figure 6). The area north and northeast of Svalbard experienced a large net positive contribution to SIC from advection of sea ice and convergence of the sea ice drift. The advection term was greatest in the west, with a maximum over the southern Yermak Plateau. The convergence term was greatest north of the passage into the Barents Sea between Nordaustlandet and Franz Josef Land.

Since the intensification term is negligible when summed over long time scales, the residual term must balance total flux divergence. As a result, the residual term, which includes concentration changes due to freezing/melting, is negative along an area extending from the Yermak Plateau in the west and past Franz Josef Land in the east. This trajectory corresponds approximately to the continental margin and the pathway of the FSAW, suggesting that sea ice is being lost over a region where warm AW is present.

3.3. Sea Ice During the Past Four Decades

The record of annual mean NSIDC SIC at the study site from 1980 to 2020 (Figure 7a) shows that sea ice concentration declined sharply during 2010–2020 relative to the three previous decades. This is also evident when considering the decadal mean SIC (M) and the decadal standard deviation of annual average SIC (σ) in the 2010s (M: 45.5%, σ: 22.6%) compared to the 1980s (M: 77.9%, σ: 12.8%), 1990s (M: 74.7%, σ: 7.6%), and 2000s (M: 67.9%, σ: 12.8%). In 2012, 2013, 2016, and 2018, annual mean SIC was below 40%, lower than any year between 1979 and 2010. This change was due to reduced SIC in both February-July and August-January. During the preceding three decades, the area was largely ice covered in spring, with mean February-July SIC greater than 75% during all years except 2006. Autumn SIC declined in the 2000s, but only once (1984) during 1980–2010 did August-January sea ice concentration fall below 10% (as opposed to 5 out of 10 years after 2010).

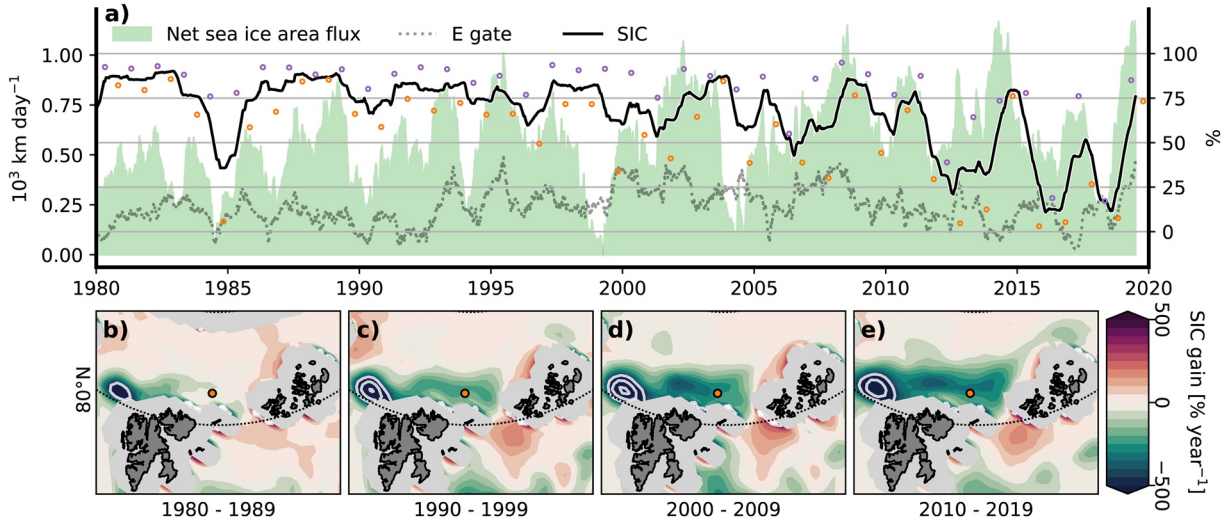

Figure 7. (a) Sea ice concentration at the shelf break mooring location (*black*) and sea ice area flux across the flux gate (*green*, flux through the E gate alone shown in black dotted line), smoothed with 365-day boxcar filters. Small circles show mean SIC for February-July (*violet*) and August-January (*orange*). (b–e) Map of the decadal mean residual term of the SIC budget. Color scale saturated at ±500% year^{-1}; beyond this, white contours are shown at intervals of 250% year^{-1}.

Sea ice area flux into the area (Figure 7a, green) increased in variability and magnitude between 1980 and 2020. After 2010, positive annual SIC anomalies were preceded by intensified sea ice area export from the north. Before 2010, interannual variability in SIC was lower, and appears largely decoupled from the time series of sea ice area flux.

Figures 7b–7e show the evolution of the SIC budget residual term (sea ice area flux divergence) from 1980 through 2019. Many features of the spatial structure of the residual term are conserved over the period; for example, the Yermak plateau stands out as a regional maximum of sea ice loss during all four decades. However, there is also some interesting evolution over the period. In particular, the region of SIC loss appears to expand eastward along the FSAW pathway - from north of Spitsbergen in the 1980s, past the study region in the 1990s and 2000s, to north of Franz Josef Land in the 2010s.

4. Summary and Discussion

4.1. Control - or Lack Thereof - of Upper Ocean Temperature on Local SIC

The seven year long record of upper ocean temperature from the continental shelf break northeast of Svalbard is dominated by a strong seasonal cycle, consistent with previous observations from the area (Ivanov et al., 2009; Pérez-Hernández et al., 2019; Renner et al., 2018). While a seasonal cycle in temperature in the FSAW core can be explained by the advection of the seasonal temperature cycle of AW in the Fram Strait (Ivanov et al., 2009; Lique & Steele, 2012), the observed spatial differences in spring ocean temperatures across the shelf slope suggest that other seasonally modulated processes also influence the ocean temperature on the shelf break: (i) the increased amplitude of the seasonal cycle on the shelf break compared to on the central slope suggests a broadening of the FSAW core and/or a greater on-shelf transport during autumn, and (ii) the near-freezing minimum temperatures near 50 m depth at the shelf break show that at this depth, spring temperature is more strongly influenced by surface processes than by the lateral advection of AW of varying temperature.

A key goal of this study was to determine whether variations in local upper ocean heat content drive interannual variability in sea ice cover. The combined records of ocean temperature and satellite-derived SIC show no evidence of such a simple relationship during the study period; strong interannual anomalies in SIC during the study period did not correspond to abnormal temperatures in the upper ocean. Notably, there was no lack of heat available in the water column at the study site during the high sea ice year of 2014, and the same was the case for the autumn of 2019 up until the end of the temperature record in mid-November.

Similarly, during the February-July season of 2017, ocean temperatures were higher than in the preceding year, yet this did not prevent sea ice concentration from remaining high for most of the period.

The lack of clear covariance between ocean temperature and sea ice concentration at the study site does not, however, imply that the sea ice state is unaffected by heating from below. During extended periods in late autumn/winter, the ocean gives off heat to the atmosphere, but a persistent sea ice cover does not form. This part of the year coincides with the warm phase of the seasonal cycle in upper ocean temperature. The combination of negative surface energy balance and heat available in the upper ocean suggests that the warm ocean temperatures act to maintain ice-free conditions during a part of the season where ice might otherwise have formed (other factors, such as the mechanical impact of winds, may also be important). The combined time series from the study period therefore suggest that upper ocean heat prevented ice formation and delayed the onset of persistent sea ice cover, but that large interannual variations in SIC were driven by factors other than ocean heat.

It is important to note that the point measurements of temperature shown here cannot necessarily be taken as a direct proxy of the near-surface ocean heat content to the north or south of the study area since cross-slope ocean gradients are relatively steep in the area (Crews et al., 2018; Pérez-Hernández et al., 2017). In addition, heat fluxes to the surface are highly dependent on the near-surface stratification (e.g., Lind et al., 2016), which we have no information about above 50 m depth.

4.2. High SIC Anomaly During Autumn 2014

Over the Arctic Ocean as a whole, surface air temperatures were anomalously low during the winter seasons of both 2013 and 2014 (Tilling et al., 2015). The total autumn sea ice volume in the Arctic was elevated during both these seasons, but the spatial pattern of sea ice extent differed markedly between 2013 and 2014, with the mean ice edge extending much farther south in the Barents and Kara Sea sections of the Arctic Ocean during autumn 2014 (Serreze et al., 2016). In the area north of Svalbard, the sea ice edge extended further west than usual in autumn this year, and average SIC at the site discussed in this manuscript was >80% from August 2014 through January 2015.

We find no indication that the local upper ocean heat content was particularly low during the 2014 August-January season, or during the preceding 2014 February-July season. We do, however, note that air temperatures were anomalously low and that, as a result, the accumulation of FDD during during the 2014 August-January season was approximately double that of the other August-January seasons. However, the low air temperatures may in part *result* from the high sea ice cover, as sea ice can have a large cooling effect on the atmosphere even at relatively small spatial scales around Svalbard (Isaksen et al., 2016). Since anomalously high SIC in late summer preceded the anomalous temperature drop (in early autumn), the anomalously high autumn SIC cannot necessarily be attributed to local sea ice growth, although it is likely that the low air temperatures contributed to additional sea ice formation (or reduced local melting from below) during that period.

In other years during the 2012–2019 period, SIC in the study area decreased between June and August. Neither the observed upper ocean temperature nor the air temperature was particularly low during these months in 2014 compared to the interannual mean. Instead, the most prominent deviation from the normal summer state in 2014 was a strong, sustained sea ice drift from the north. This unusually large sea ice area flux into the study area began in the end of July and reached a maximum in mid-August, and sea ice drift into the area remained relatively high through autumn 2014. We conclude that the continued supply of sea ice advected from the north counteracted the seasonal melting, and prevented the disappearance of the sea ice north of Svalbard during late summer 2014. The resulting reduced heat flux from the ocean to the atmosphere resulted in an unusually rapid cooling of the air, which in turn may have contributed to reduced melting and increased sea ice growth during the rest of 2014.

An examination of the large-scale sea ice drift pattern (Figure 5) indicates that the flow of the Transpolar Drift Stream was deflected toward the left during summer 2014, with its mean exit pathway shifting eastward away from the Fram Strait and toward the study region northeast of Svalbard. As a result, large amounts of sea ice were advected from the central Arctic Ocean southwards toward the study area and further south into the Barents Sea. While drivers of large-scale sea ice motion are beyond the scope of

this study, we note that previous studies have related similar drift anomalies to variations in the sea level pressure distribution across the Arctic Ocean and the Barents Sea (Arfeuille et al., 2000; Kwok, 2009). We conclude that the high summer and autumn SIC in the region north of Svalbard and in the Barents Sea during 2014 was a regional expression of atmospherically driven variations in large-scale sea ice advection patterns, rather than a result of local processes.

4.3. Low SIC Anomalies During Spring 2016 and 2018

Sea ice concentration north and northeast of Svalbard was abnormally low during the winter/spring seasons of 2016 and 2018. During both years, the mean 30% SIC edge along the continental slope was located to the east of the study site. Ocean temperatures were higher than the interannual mean during both periods, suggesting that anomalously large heat content may have contributed to limiting ice formation. However, ocean temperatures also remained relatively high between these two seasons, including during the high SIC spring of 2017. Likewise, mean ocean temperature near the AW core, at 107 m depth, was higher during high SIC in February-July of 2015 than during the low-SIC season in the following year. Our observations do not, therefore, support the attribution of the low sea ice concentrations in 2016 and 2018 to increased ocean heat content alone.

The 2016 spring season was a period of anomalously high air temperatures and low sea ice extent across the Arctic Ocean (Ricker, Hendricks, Girard-Ardhuin, et al., 2017; Petty et al., 2018). The anomalies in air temperature and SIC were both intensified in the eastern Atlantic sector of the Arctic Ocean (Cullather et al., 2016; Perovich et al., 2016), and the onset of melt in the northern Barents Sea (directly south of the study area) occurred earlier than ever before in the satellite record, nearly a month earlier than the 1981–2010 mean (J. Stroeve & Notz, 2018). The high surface air temperatures in the beginning of the year have been attributed in part to an atmospheric low-pressure system that brought heat and moisture into the Barents and Kara Sea region in late December 2015 (Boisvert et al., 2016; Cullather et al., 2016). After 2016, 2018 was the second warmest year in the Arctic in modern times (Overland et al., 2018). Arctic sea ice was low in 2018, particularly during the winter season, but the negative anomaly was not centered in the Barents-Kara Sea sector to the same degree as during 2016 (Perovich et al., 2018).

At the study site, the 2016 and 2018 low sea ice anomalies coincided with interannual February-July minima both in sea ice advection (64% and 32% of the 2013–2019 mean, respectively) and number of freezing degree days (52% and 76.2% of the 2013–2019 mean). The latter suggests that the potential for local sea ice formation was much less than usual during these years. As discussed in Section 4.2 and in Onarheim et al. (2014), air temperature and sea ice concentration are closely related through a feedback cycle, and the relatively low flux of sea ice into the area will likely have contributed to higher local air temperatures and less local sea ice formation. However, the large geographic extents of the sea ice and temperature anomalies again suggest that the processes responsible for the negative SIC anomalies in 2016 and 2018 are large-scale, and cannot be explained by local processes specific to the AW inflow region alone.

Although we find no evidence that the negative SIC anomalies in spring occurred as a result of an unusually warm upper ocean, we note that ocean temperatures near 50 m depth were anomalously high during the spring seasons of 2016–2018. These years stand out in that the ocean did not reach near-freezing temperatures for extended periods of time. This could suggest a reduced modification of the upper layer by ice-ocean interactions during low-SIC years, although the high temperatures in spring 2017 appears to contradict this interpretation.

Upper ocean temperatures were anomalously high in autumn 2016, *following* the unusually ice-free spring. We speculate that the high ocean temperatures in autumn occured as a result of the reduced sea ice cover during the preceding season - through increased atmosphere-ocean heat flux in summer, and possibly increased vertical mixing of the upper ocean. Several authors (e.g., Danielson et al., 2020; Serreze & Barry, 2011; Timmermans, 2015) have discussed how increased warming during lower SIC conditions in spring may lead to further reduced ice cover the following year. However, seeing that spring 2017 was a normal season in the study area in terms of SIC, the observed increased ocean temperatures may not have been sufficiently high to impact sea ice formation and/or sea ice survival in the study region - or the excess heat was already redistributed or advected downstream. This interpretation is further complicated by the absence of

high autumn temperatures in the upper ocean in 2018 - suggesting that autumn upper ocean heat content is not simply a function of sea ice cover during the preceding spring in this strongly advection-influenced region.

4.4. A Changing Background Sea Ice State

The record of sea ice concentration at the study site since 1980 suggests that a regime change took place in the region around 2010. In the following decade, average sea ice concentration in both spring and autumn were low relative to previous decades. Sea ice variability also increased in the 2010s, resulting in large interannual SIC anomalies as described in the previous sections, and sea ice area flux from the north became greater and more variable between 1980 and 2020.

The sea ice decline in the region north of Svalbard is well documented (e.g., Onarheim et al., 2014; Polyakov et al., 2017; Tetzlaff et al., 2014). As well as the decrease in sea ice concentration, the region has experienced a reduction in multiyear ice (J. C. Stroeve et al., 2018), which now rarely occurs in the region north of Svalbard (Renner et al., 2013). As a result of thinning, sea ice has become more mobile, and drift velocities have increased across the Arctic Ocean (Kwok et al., 2013). The increased magnitude and variability of sea ice area advection from the north into the study region since 1980 is likely an expression of this change.

As the sea ice edge moved eastward during recent decades, so did the region of sea ice area flux convergence, as shown by the location of the region of negative values of the SIC budget residual extending progressively farther east along the pathway of the FSAW from the 1980s to the 2010s (Figure 7). This suggests that the area that is actively maintained ice-free by the ocean during parts of the year has expanded, and that the influence of Atlantic Water on sea ice cover is expanding into the Arctic Ocean, consistent with other studies (e.g., Ivanov et al., 2012; Polyakov et al., 2017).

Our study suggests that sea ice drift from the north, rather than variations in ocean heat content, was the main driver of interannual variability of local sea ice concentration in the study region during 2012–2019. However, the large net sea ice area flux divergence, and the extended periods of low ice concentrations despite low air temperature in autumn, suggest that melting from below by the ocean must be key to maintaining the ocean wholly or partially ice-free through large parts of the year. Our findings are consistent with a recent study from the AW inflow region north of Svalbard (Duarte et al., 2020), which showed that warm AW can very effectively melt ice which is advected into the area (although in a region further upstream, with more and warmer shallow AW).

The active melting of sea ice also impacts the near-surface layer of the ocean north of Svalbard, reducing temperature and salinity and increasing upper ocean stratification (Rudels, 2016). The upper ocean temperature records from the shelf break mooring show increased vertical gradients and often near-freezing temperatures during high sea ice concentrations. This indicates that the properties of the upper ∼50 m of the water column are strongly modified by ice melt and/or formation. The smaller amplitude of the annual temperature cycle at the slope mooring suggests that ice-ocean interactions exert a lesser influence on the local water column near the core of the AW inflow, where currents are stronger than further up-slope, consistent with faster rates of replenishment of AW from the west and advection of modified surface water toward the east. In the northern Barents Sea, melting of sea ice has a lasting imprint on the upper ocean layer, and acts to provide favorable conditions for sea ice formation during the following growth season (Ellingsen et al., 2009; Lind et al., 2018). This is less likely to be the case in the AW inflow region north of Svalbard, which is continuously replenished by the inflow from the west, and therefore has a shorter “memory” of previous sea ice states.

5. Conclusions

Sea ice concentration is determined by a combination of local sea ice formation, melting from above and below, breaking and deformation by external and internal stresses, and lateral ice advection. The present study highlights the importance of the latter north of Svalbard; advective terms dominate the local SIC budget, and examination of the time series suggest that drift of ice from the north and east excerts a primary control on SIC variability in the region.

Variations in SIC driven by sea ice advection strongly impact regional surface air temperature. In this study, heat flux from the ocean to the atmosphere decreased markedly during high SIC conditions, and episodes of sea ice advection into the area were typically followed by a cooling of the air. In addition to air temperature, interannual sea ice variability north of Svalbard has the potential to impact ecosystem dynamics (Post et al., 2013) and human activities (Silber & Adams, 2019; Stocker et al., 2020), and the successful prediction of seasonal sea ice concentration in the region could be of use to, for example, fisheries management and tourism operators in the area. This study implies that large-scale sea ice advection from the north, which may be associated with specific atmospheric configurations over the Arctic Ocean, is a primary driver of interannual sea ice along the FSAW pathway north of Svalbard. It may therefore also be the variable with the greatest predictive potential for the the sea ice state in the region from year to year, and interannual sea ice predictability may ultimately be limited by the predictability of the large-scale atmosphere over the Atlantic sector of the Arctic Ocean. The anomalously high SIC during autumn of 2014, which was associated with strong ice flux from the north, extended well into the Barents Sea, highlighting the impact of southward sea ice drift on variability in the Barents Sea as well as along the FSAW pathway.

The strong reduction in ocean-atmosphere heat flux during high SIC years likely results in a relative increase in the temperature of the ocean water that is transported downstream with the FSAW. All else being equal, ocean heat transport with the Atlantic Water Boundary Current (including lateral heat losses into the the interior Arctic Ocean) may therefore increase during years with anomalously high sea ice advection into the region north of Svalbard - and vice versa. As such, interannual sea ice variability may contribute to interannual ocean temperature variability further east along the flow pathway (influencing for example year-to-year changes in AW heat transport as observed on the continental slope in the Laptev Sea; Pnyushkov et al., 2018). The implications of such a mechanism, and of the increasingly open area associated with the eastward migration of the marginal ice zone along the pathway of the FSAW, are unclear, but highlight the need for an increased understanding of the many complex interactions between ocean, ice, and atmosphere in order to understand how the Arctic Ocean system may evolve in the future.

Budget analysis of SIC suggests that the region north of Svalbard is an important sink of sea ice that is advected into the area. The spatial distribution of negative values of the residual term, a proxy for local sea ice loss due to melting and deformation, coincides with the inflow path of the warm FSAW along the continental slope of the southern Nansen Basin. In contrast, the northern Barents Sea, a region dominated by cold Arctic Water rather than AW (e.g., Lind & Ingvaldsen, 2012), emerges as a SIC *source*. Since SIC is a non-conservative quantity, the area budget methodology cannot be used to estimate mass loss/melt rates, but the spatial relationship between the SIC residual term and the large-scale ocean temperature distribution clearly demonstrates the importance of oceanic heat advection for sea ice distribution in the region. The extended periods of low SIC, heat loss from the surface ocean, and warm ocean temperatures during late autumn/winter in most years also suggest that the relatively long ice-free season is a result of ocean influence. The fact that we find little evidence of interannual fluctuations in upper ocean heat driving interannual SIC variability is likely a result of the much higher year-to-year variability in sea ice advection and atmospheric factors compared to variability in ocean heat content on interannual scales. Long-term changes in ocean temperature, or major shifts in the ocean circulation, remain likely to have a strong impact on SIC along the inflow pathways of AW into the Arctic Ocean (Årthun et al., 2019; Polyakov et al., 2017).

Data Availability Statement

A-TWAIN mooring data are openly available from the Norwegian Polar Data Centre: https://doi.org/10.21334/npolar.2017.73d0ea3a, https://doi.org/10.21334/npolar.2020.c972dd9c, https://data.npolar.no/dataset/ceb74f92-bb58-44f0-b492-c75667ddc86d, and https://data.npolar.no/dataset/e7041026-9d91-4924-a186-48ba2d93b487.

Acknowledgments
We thank the captains and crews of RV Lance and RV Kronprins Haakon, and NPI and IMR personnel for technical support with the mooring deployments and cruises. The A-TWAIN project (project number 66050) is financially supported by the Fram Centre flagship "Sea ice in the Arctic Ocean, technology and agreements." The analysis was funded by the Research Council of Norway through the Nansen Legacy project (RCN 276730).

References

Aagaard, K., Coachman, L. K., & Carmack, E. (1981). On the halocline of the Arctic Ocean. *Deep Sea Research A. Oceanographic Research Papers*, *28*(6), 529–545. https://doi.org/10.1016/0198-0149(81)90115-1

Arfeuille, G., Mysak, L. A., & Tremblay, L.-B. (2000). Simulation of the interannual variability of the wind-driven Arctic sea-ice cover during 1958-1998. *Climate Dynamics*, *16*(2), 107–121. https://doi.org/10.1007/PL00013732

Årthun, M., Eldevik, T., & Smedsrud, L. H. (2019). The Role of Atlantic Heat Transport in Future Arctic Winter Sea Ice Loss. *Journal of Climate*, *32*(11), 3327–3341. https://doi.org/10.1175/JCLI-D-18-0750.1

Boisvert, L. N., Petty, A. A., & Stroeve, J. C. (2016). The Impact of the Extreme Winter 2015/16 Arctic Cyclone on the Barents-Kara Seas. *Monthly Weather Review*, *144*(11), 4279–4287. https://doi.org/10.1175/MWR-D-16-0234.1

Cavalieri, D. J., Parkinson, C. L., Gloersen, P., & Zwally, H. J. (1996). *Sea ice concentrations from Nimbus-7 SMMR and DMSP SSM/I-SSMIS passive Microwave data, Version 1. Northern Hemispere subset*. NASA National Snow and Ice Data Center Distributed Active Archive Center. https://doi.org/10.5067/8GQ8LZQVL0VL

Cokelet, E. D., Tervalon, N., & Bellingham, J. G. (2008). Hydrography of the West Spitsbergen Current, Svalbard Branch: Autumn 2001. *Journal of Geophysical Research*, *113*(C1). https://doi.org/10.1029/2007JC004150

Comiso, J. C., Meier, W. N., & Gersten, R. (2017). Variability and trends in the Arctic Sea ice cover: Results from different techniques. *Journal of Geophysical Research: Oceans*, *122*(8), 6883–6900. https://doi.org/10.1002/2017JC012768

Copernicus Climate Change Service (C3S). (2017). *ERA5: Fifth generation of ECMWF atmospheric reanalyzes of the global climate Copernicus climate change Service climate data Store (CDS)*. https://cds.climate.copernicus.eu/cdsapp#!/home

Crews, L., Sundfjord, A., Albretsen, J., & Hattermann, T. (2018). Mesoscale Eddy Activity and Transport in the Atlantic Water Inflow Region North of Svalbard. *Journal of Geophysical Research: Oceans*, *123*(1), 201–215. https://doi.org/10.1002/2017JC013198

Cullather, R. I., Lim, Y.-K., Boisvert, L. N., Brucker, L., Lee, J. N., & Nowicki, S. M. J. (2016). Analysis of the warmest Arctic winter, 2015-2016. *Geophysical Research Letters*, *43*(20), 808–810. https://doi.org/10.1002/2016GL071228

Danielson, S. L., Ahkinga, O., Ashjian, C., Basyuk, E., Cooper, L. W., Eisner, L., et al. (2020). Manifestation and consequences of warming and altered heat fluxes over the Bering and Chukchi Sea continental shelves. *Deep Sea Research Part II: Topical Studies in Oceanography*, *177*, 104781. https://doi.org/10.1016/j.dsr2.2020.104781

Duarte, P., Sundfjord, A., Meyer, A., Hudson, S. R., Spreen, G., & Smedsrud, L. H. (2020). Warm Atlantic Water Explains Observed Sea Ice Melt Rates North of Svalbard. *Journal of Geophysical Research: Oceans*, *125*(8), e2019JC015662. https://doi.org/10.1029/2019JC015662

Ellingsen, I., Slagstad, D., & Sundfjord, A. (2009). Modification of water masses in the Barents Sea and its coupling to ice dynamics: A model study. *Ocean Dynamics*, *59*(6), 1095–1108. https://doi.org/10.1007/s10236-009-0230-5

England, M., Jahn, A., & Polvani, L. (2019). Nonuniform Contribution of Internal Variability to Recent Arctic Sea Ice Loss. *Journal of Climate*, *32*(13), 4039–4053. https://doi.org/10.1175/JCLI-D-18-0864.1

Gjelten, H. M., Nordli, Ø., Isaksen, K., Førland, E. J., Sviashchennikov, P. N., Wyszynski, P., et al. (2016). Air temperature variations and gradients along the coast and fjords of western Spitsbergen. *Polar Research*, *35*(1), 29878. https://doi.org/10.3402/polar.v35.29878

Graham, R. M., Itkin, P., Meyer, A., Sundfjord, A., Spreen, G., Smedsrud, L. H., et al. (2019). Winter storms accelerate the demise of sea ice in the Atlantic sector of the Arctic Ocean. *Scientific Reports*, *9*(1), 9222. https://doi.org/10.1038/s41598-019-45574-5

Grunseich, G., & Wang, B. (2016). Predictability of Arctic Annual Minimum Sea Ice Patterns. *Journal of Climate*, *29*(19), 7065–7088. https://doi.org/10.1175/JCLI-D-16-0102.1

Holland, P. R., & Kimura, N. (2016). Observed Concentration Budgets of Arctic and Antarctic Sea Ice. *Journal of Climate*, *29*(14), 5241–5249. https://doi.org/10.1175/JCLI-D-16-0121.1

Isaksen, K., Nordli, Ø., Førland, E. J., Łupikasza, E., Eastwood, S., & Niedźwiedź, T. (2016). Recent warming on Spitsbergen-Influence of atmospheric circulation and sea ice cover. *Journal of Geophysical Research - D: Atmospheres*, *121*(20), 11,913–11,931. https://doi.org/10.1002/2016JD025606

Ivanov, V., Alexeev, V., Koldunov, N. V., Repina, I., Sandø, A. B., Smedsrud, L. H., & Smirnov, A. (2016). Arctic Ocean Heat Impact on Regional Ice Decay: A Suggested Positive Feedback. *Journal of Physical Oceanography*, *46*(5), 1437–1456. https://doi.org/10.1175/JPO-D-15-0144.1

Ivanov, V. V., Alexeev, V. A., Repina, I., Koldunov, N. V., & Smirnov, A. (2012). Tracing Atlantic Water Signature in the Arctic Sea Ice Cover East of Svalbard. *Advances in Meteorology*, *2012*, 1–11. https://doi.org/10.1155/2012/201818

Ivanov, V. V., Polyakov, I. V., Dmitrenko, I. A., Hansen, E., Repina, I. A., Kirillov, S. A., et al. (2009). Seasonal variability in Atlantic Water off Spitsbergen. *Deep Sea Research I: Oceanographic Research Papers*, *56*(1), 1–14. https://doi.org/10.1016/j.dsr.2008.07.013

Ivanov, V. V., & Repina, I. A. (2018). The Effect of Seasonal Variability of Atlantic Water on the Arctic Sea Ice Cover. *Izvestiya, Atmospheric and Oceanic Physics*, *54*(1), 65–72. https://doi.org/10.1134/S0001433818010061

Jakobsson, M., Mayer, L., Coakley, B., Dowdeswell, J. A., Forbes, S., Fridman, B., et al. (2012). The International Bathymetric Chart of the Arctic Ocean (IBCAO) Version 3.0. *Geophysical Research Letters*, *39*(12). https://doi.org/10.1029/2012GL052219

Kaur, S., Ehn, J. K., & Barber, D. G. (2018). Pan-arctic winter drift speeds and changing patterns of sea ice motion: 1979-2015. *Polar Record*, *54*(5–6), 303–311. https://doi.org/10.1017/S0032247418000566

Kawasaki, T., & Hasumi, H. (2016). The inflow of A tlantic water at the F ram S trait and its interannual variability. *Journal of Geophysical Research: Oceans*, *121*(1), 502–519. https://doi.org/10.1002/2015JC011375

Kimura, N., Nishimura, A., Tanaka, Y., & Yamaguchi, H. (2013). Influence of winter sea-ice motion on summer ice cover in the Arctic. *Polar Research*, *32*(1), 20193. https://doi.org/10.3402/polar.v32i0.20193

Koenig, Z., Provost, C., Sennéchael, N., Garric, G., & Gascard, J. C. (2017). The Yermak Pass Branch: A Major Pathway for the Atlantic Water North of Svalbard? *Journal of Geophysical Research: Oceans*, *122*(12), 9332–9349. https://doi.org/10.1002/2017JC013271

Krumpen, T., Belter, H. J., Boetius, A., Damm, E., Haas, C., Hendricks, S., et al. (2019). Arctic warming interrupts the Transpolar Drift and affects long-range transport of sea ice and ice-rafted matter. *Scientific Reports*, *9*(1), 1–9. https://doi.org/10.1038/s41598-019-41456-y

Kwok, R. (2009). Outflow of Arctic Ocean Sea Ice into the Greenland and Barents Seas: 1979-2007. *Journal of Climate*, *22*(9), 2438–2457. https://doi.org/10.1175/2008JCLI2819.1

Kwok, R. (2015). Sea ice convergence along the Arctic coasts of Greenland and the Canadian Arctic Archipelago: Variability and extremes (1992-2014). *Geophysical Research Letters*, *42*(18), 7598–7605. https://doi.org/10.1002/2015GL065462

Kwok, R. (2018). Arctic sea ice thickness, volume, and multiyear ice coverage: Losses and coupled variability (1958-2018). *Environmental Research Letters*, *13*(10), 105005. https://doi.org/10.1088/1748-9326/aae3ec

Kwok, R., Spreen, G., & Pang, S. (2013). Arctic sea ice circulation and drift speed: Decadal trends and ocean currents. *Journal of Geophysical Research: Oceans*, *118*(5), 2408–2425. https://doi.org/10.1002/jgrc.20191

Lind, S., & Ingvaldsen, R. B. (2012). Variability and impacts of Atlantic Water entering the Barents Sea from the north. *Deep Sea Research Part I: Oceanographic Research Papers*, *62*, 70–88. https://doi.org/10.1016/j.dsr.2011.12.007

Lind, S., Ingvaldsen, R. B., & Furevik, T. (2016). Arctic layer salinity controls heat loss from deep Atlantic layer in seasonally ice-covered areas of the Barents Sea. *Geophysical Research Letters*, *43*(10), 5233–5242. https://doi.org/10.1002/2016GL068421

Lind, S., Ingvaldsen, R. B., & Furevik, T. (2018). Arctic warming hotspot in the northern Barents Sea linked to declining sea-ice import. *Nature Climate Change*, *8*(7), 634–639. https://doi.org/10.1038/s41558-018-0205-y

Lique, C., & Steele, M. (2012). Where can we find a seasonal cycle of the Atlantic water temperature within the Arctic Basin? *Journal of Geophysical Research*, *117*(C3). https://doi.org/10.1029/2011JC007612

Lundesgaard, Ø., Sundfjord, A., Renner, A. H. H., & Beszczynska-Möller, A. (2020a). *A-TWAIN mooring data 2015-2017 [Data set]*. Norwegian Polar Institute. https://doi.org/10.21334/npolar.2020.ceb74f92

Lundesgaard, Ø., Sundfjord, A., Renner, A. H. H., & Beszczynska-Möller, A. (2020b). *A-TWAIN mooring data 2017-2019 [Data set]*. Norwegian Polar Institute. https://doi.org/10.21334/npolar.2020.e7041026

Menze, S., Ingvaldsen, R. B., Haugan, P., Fer, I., Sundfjord, A., Beszczynska-Moeller, A., & Falk-Petersen, S. (2019). Atlantic Water Pathways Along the North-Western Svalbard Shelf Mapped Using Vessel-Mounted Current Profilers. *Journal of Geophysical Research: Oceans*, *124*(3), 1699–1716. https://doi.org/10.1029/2018JC014299

Merkouriadi, I., Cheng, B., Hudson, S. R., & Granskog, M. A. (2020). Effect of frequent winter warming events (storms) and snow on sea-ice growth - a case from the Atlantic sector of the Arctic Ocean during the N-ICE2015 campaign. *Annals of Glaciology*, *61*, 164–170. https://doi.org/10.1017/aog.2020.25

Meyer, A., Fer, I., Sundfjord, A., & Peterson, A. K. (2018). Mixing rates and vertical heat fluxes north of Svalbard from Arctic winter to spring. *Journal of Geophysical Research: Oceans*, 4569–4586. https://doi.org/10.1002/2016JC012441@10.1002/(ISSN)2169-9291.NICE1

Moritz, R. E., Bitz, C. M., & Steig, E. J. (2002). Dynamics of Recent Climate Change in the Arctic. *Science*, *297*(5586), 1497–1502. https://doi.org/10.1126/science.1076522

Muilwijk, M., Smedsrud, L. H., Ilicak, M., & Drange, H. (2018). Atlantic Water Heat Transport Variability in the 20th Century Arctic Ocean From a Global Ocean Model and Observations. *Journal of Geophysical Research: Oceans*, *123*(11), 8159–8179. https://doi.org/10.1029/2018JC014327

Nordli, Ø., Przybylak, R., Ogilvie, A. E. J., & Isaksen, K. (2014). Long-term temperature trends and variability on Spitsbergen: The extended Svalbard Airport temperature series, 1898-2012. *Polar Research*, *33*(1), 21349. https://doi.org/10.3402/polar.v33.21349

Olonscheck, D., Mauritsen, T., & Notz, D. (2019). Arctic sea-ice variability is primarily driven by atmospheric temperature fluctuations. *Nature Geoscience*, *12*(6), 430–434. https://doi.org/10.1038/s41561-019-0363-1

Onarheim, I. H., Eldevik, T., Smedsrud, L. H., & Stroeve, J. C. (2018). Seasonal and Regional Manifestation of Arctic Sea Ice Loss. *Journal of Climate*, *31*(12), 4917–4932. https://doi.org/10.1175/JCLI-D-17-0427.1

Onarheim, I. H., Smedsrud, L. H., Ingvaldsen, R. B., & Nilsen, F. (2014). Loss of sea ice during winter north of Svalbard. *Tellus A: Dynamic Meteorology and Oceanography*, *66*(1), 23933. https://doi.org/10.3402/tellusa.v66.23933

Overland, J. E., Hanna, E., Hanssen-Bauer, I., Kim, S. J., Walsh, J. E., Wang, M., et al. (2018). *Surface air temperature [in Arctic Report card 2018]*. Retrieved from https://www.arctic.noaa.gov/Report-Card

Pérez-Hernández, M. D., Pickart, R. S., Pavlov, V., Våge, K., Ingvaldsen, R., Sundfjord, A., et al. (2017). The Atlantic Water boundary current north of Svalbard in late summer. *Journal of Geophysical Research: Oceans*, *122*(3), 2269–2290. https://doi.org/10.1002/2016JC012486

Pérez-Hernández, M. D., Pickart, R. S., Torres, D. J., Bahr, F., Sundfjord, A., Ingvaldsen, R., et al. (2019). Structure, Transport, and Seasonality of the Atlantic Water Boundary Current North of Svalbard: Results From a Yearlong Mooring Array. *Journal of Geophysical Research: Oceans*, *124*(3), 1679–1698. https://doi.org/10.1029/2018JC014759

Perovich, D. K., Meier, W., Tschudi, M., Farrell, S., Gerland, S., Hendricks, S., et al. (2016). *Sea ice [in Arctic Report card 2016]*. Retrieved from http://www.arctic.noaa.gov/Report-Card

Perovich, D. K., Meier, W., Tschudi, M., Farrell, S., Hendricks, S., Gerland, S., et al. (2018). *Sea ice [in Arctic Report card 2018]*. Retrieved from http://www.arctic.noaa.gov/Report-Card

Perovich, D. K., & Richter-Menge, J. A. (2015). Regional variability in sea ice melt in a changing Arctic. *Philosophical Transactions of the Royal Society A*, *373*(2045), 20140165. https://doi.org/10.1098/rsta.2014.0165

Petty, A. A., Stroeve, J. C., Holland, P. R., Boisvert, L. N., Bliss, A. C., Kimura, N., & Meier, W. N. (2018). The Arctic sea ice cover of 2016: A year of record-low highs and higher-than-expected lows. *The Cryosphere*, *12*(2), 433–452. https://doi.org/10.5194/tc-12-433-2018

Pnyushkov, A. V., Polyakov, I. V., Rember, R., Ivanov, V. V., Alkire, M. B., Ashik, I. M., et al. (2018). Heat, salt, and volume transports in the eastern Eurasian Basin of the Arctic Ocean from 2 years of mooring observations. *Ocean Science*, *14*(6), 1349–1371. https://doi.org/10.5194/os-14-1349-2018

Polyakov, I. V., Pnyushkov, A. V., Alkire, M. B., Ashik, I. M., Baumann, T. M., Carmack, E. C., et al. (2017). Greater role for Atlantic inflows on sea-ice loss in the Eurasian Basin of the Arctic Ocean. *Science*, *356*(6335), 285–291. https://doi.org/10.1126/science.aai8204

Post, E., Bhatt, U. S., Bitz, C. M., Brodie, J. F., Fulton, T. L., Hebblewhite, M., et al. (2013). Ecological Consequences of Sea-Ice Decline. *Science*, *341*(6145), 519–524. https://doi.org/10.1126/science.1235225

Renner, A. H. H., Hendricks, S., Gerland, S., Beckers, J., Haas, C., & Krumpen, T. (2013). Large-scale ice thickness distribution of first-year sea ice in spring and summer north of Svalbard. *Annals of Glaciology*, *54*(62), 13–18. https://doi.org/10.3189/2013AoG62A146

Renner, A. H. H., Sundfjord, A., Janout, M. A., Ingvaldsen, R. B., Beszczynska-Möller, A., Pickart, R. S., & Pérez-Hernández, M. D. (2018). Variability and Redistribution of Heat in the Atlantic Water Boundary Current North of Svalbard. *Journal of Geophysical Research: Oceans*, *123*(9), 6373–6391. https://doi.org/10.1029/2018JC013814

Ricker, R., Hendricks, S., Girard-Ardhuin, F., Kaleschke, L., Lique, C., Tian-Kunze, X., et al. (2017). Satellite-observed drop of Arctic sea ice growth in winter 2015-2016. *Geophysical Research Letters*, *44*(7), 3236–3245. https://doi.org/10.1002/2016GL072244

Ricker, R., Hendricks, S., Kaleschke, L., Tian-Kunze, X., King, J., & Haas, C. (2017). A weekly Arctic sea-ice thickness data record from merged CryoSat-2 and SMOS satellite data. *The Cryosphere*, *11*(4), 1607–1623. https://doi.org/10.5194/tc-11-1607-2017

Rigor, I. G., Wallace, J. M., & Colony, R. L. (2002). Response of Sea Ice to the Arctic Oscillation. *Journal of Climate*, *15*(18), 2648–2663. https://doi.org/10.1175/1520-0442(2002)015⟨2648:ROSITT⟩2.0.CO;2

Rinke, A., Maturilli, M., Graham, R. M., Matthes, H., Handorf, D., Cohen, L., et al. (2017). Extreme cyclone events in the Arctic: Wintertime variability and trends. *Environmental Research Letters*, *12*(9), 094006. https://doi.org/10.1088/1748-9326/aa7def

Rudels, B. (2016). Arctic Ocean stability: The effects of local cooling, oceanic heat transport, freshwater input, and sea ice melt with special emphasis on the Nansen Basin. *Journal of Geophysical Research: Oceans*, *121*(7), 4450–4473. https://doi.org/10.1002/2015JC011045

Rudels, B., Björk, G., Nilsson, J., Winsor, P., Lake, I., & Nohr, C. (2005). The interaction between waters from the Arctic Ocean and the Nordic Seas north of Fram Strait and along the East Greenland Current: Results from the Arctic Ocean-02 Oden expedition. *Journal of Marine Systems*, *55*(1), 1–30. https://doi.org/10.1016/j.jmarsys.2004.06.008

Serreze, M. C., & Barry, R. G. (2011). Processes and impacts of Arctic amplification: A research synthesis. *Global and Planetary Change*, *77*(1), 85–96. https://doi.org/10.1016/j.gloplacha.2011.03.004

Serreze, M. C., & Stroeve, J. (2015). Arctic sea ice trends, variability and implications for seasonal ice forecasting. *Philosophical Transactions of the Royal Society A*, *373*(2045), 20140159. https://doi.org/10.1098/rsta.2014.0159

Serreze, M. C., Stroeve, J., Barrett, A. P., & Boisvert, L. N. (2016). Summer atmospheric circulation anomalies over the Arctic Ocean and their influences on September sea ice extent: A cautionary tale. *Journal of Geophysical Research - D: Atmospheres*, *121*(19), 11,463–11,485. https://doi.org/10.1002/2016JD025161

Silber, G. K., & Adams, J. D. (2019). Vessel Operations in the Arctic, 2015-2017. *Frontiers in Marine Science*, *6*. https://doi.org/10.3389/fmars.2019.00573

Sorteberg, A., & Walsh, J. E. (2008). Seasonal cyclone variability at 70°N and its impact on moisture transport into the Arctic. *Tellus*, *60*, 570–586. https://doi.org/10.1111/j.1600-0870.2008.00314.x

Spreen, G., Kaleschke, L., & Heygster, G. (2008). Sea ice remote sensing using AMSR-E 89-GHz channels. *Journal of Geophysical Research*, *113*(C2). https://doi.org/10.1029/2005JC003384

Stocker, A. N., Renner, A. H. H., & Knol-Kauffman, M. (2020). Sea ice variability and maritime activity around Svalbard in the period 2012-2019. *Scientific Reports*, *10*(1), 17043, October. https://doi.org/10.1038/s41598-020-74064-2

Stroeve, J. C., Schroder, D., Tsamados, M., & Feltham, D. (2018). Warm winter, thin ice? *The Cryosphere*, *12*(5), 1791–1809. https://doi.org/10.5194/tc-12-1791-2018

Stroeve, J., & Notz, D. (2018). Changing state of Arctic sea ice across all seasons. *Environmental Research Letters*, *13*(10), 103001. https://doi.org/10.1088/1748-9326/aade56

Sundfjord, A., Lundesgaard, Ø., Renner, A. H. H., Beszczynska-Möller, A., & Pnyushkov, A. (2020). *A-TWAIN mooring data 2013-2015 [Data set]*. Norwegian Polar Institute. https://doi.org/10.21334/npolar.2020.c972dd9c

Sundfjord, A., Renner, A. H. H., & Beszczynska-Möller, A. (2017). *A-TWAIN mooring hydrography and current data Sep 2012 - Sep 2013 [Data set]*. Norwegian Polar Institute. https://doi.org/10.21334/npolar.2017.73d0ea3a

Tetzlaff, A., Lüpkes, C., Birnbaum, G., Hartmann, J., Nygård, T., & Vihma, T. (2014). Brief Communication: Trends in sea ice extent north of Svalbard and its impact on cold air outbreaks as observed in spring 2013. *The Cryosphere*, *8*(5), 1757–1762. https://doi.org/10.5194/tc-8-1757-2014

Tilling, R. L., Ridout, A., Shepherd, A., & Wingham, D. J. (2015). Increased Arctic sea ice volume after anomalously low melting in 2013. *Nature Geoscience*, *8*(8), 643–646. https://doi.org/10.1038/ngeo2489

Timmermans, M.-L. (2015). The impact of stored solar heat on Arctic sea ice growth. *Geophysical Research Letters*, *42*(15), 6399–6406. https://doi.org/10.1002/2015GL064541

Tschudi, M., Meier, W. N., Stewart, J. S., Fowler, C., & Maslanik, J. (2019). *Polar Pathfinder daily 25 km EASE-Grid Sea ice motion vectors, Version 4 (hourly, single levels)*. NASA National Snow and Ice Data Center Distributed Active Archive Center. https://doi.org/10.1029/2018JC014299

Wang, C., Graham, R. M., Wang, K., Gerland, S., & Granskog, M. A. (2019). Comparison of ERA5 and ERA-Interim near-surface air temperature, snowfall and precipitation over Arctic sea ice: Effects on sea ice thermodynamics and evolution. *The Cryosphere*, *13*(6), 1661–1679. https://doi.org/10.5194/tc-13-1661-2019